nature communications

Article

https://doi.org/10.1038/s41467-025-67886-z

Epitaxial growth of wafer-scale 2D superconductor single crystals by metal-organic chemical vapor deposition

Received: 31 July 2025

Accepted: 11 December 2025

Published online: 21 December 2025

Zhenyu Wang[1,2,3,4,7], Tan Luo[1,2,7], Liu Shi[1,2,7], Xin Chen[4,7], Jing Zhang[5,6], Zhiwei Yao[1,2], Jianzhou Lu[1,2], Yiou Huang[1,2], Zheng Zhu[1,2], Le Zheng[1,2], Mengjiao Li[1,2], Andras Kis[3,4], Lei Zhang[1,2] & Jianhua Zhang[1,2]

Metallic two-dimensional (2D) transition metal dichalcogenides (TMDCs) are garnering significant attention for their ability to enhance device performance when used as 2D contacts with semiconducting 2D materials, as well as for their intriguing low-temperature properties, including superconductivity, magnetism, and charge density waves (CDWs). However, the advancement of both fundamental studies and practical applications has been hindered by challenges in synthesizing high-quality, large-area materials. In this work, we report the epitaxial growth of wafer-scale 2D superconducting TMDC single-crystal multilayers by metal–organic chemical vapor deposition (MOCVD). Our NbS_2 multilayer films achieve high wafer-scale uniformity and single crystallinity of 2H phase, as confirmed by AFM, Raman spectroscopy, SHG mapping, LEED and STEM measurements. This is enabled by a dual-precursor strategy that drives self-templated concurrent epitaxy on lattice-matched sapphire, which is further supported by a kinetic growth model. Devices fabricated from the NbS_2 film demonstrate superconductivity below a transition temperature of 3 K, consistent with a Berezinskii-Kosterlitz-Thouless (BKT) type superconducting phase transition, with an impressive yield of 95.1% and a resistance variation of only 12%. Additionally, we demonstrate the wafer-scale growth of superconducting $NbSe_2$ films ($T_c = 5$ K) via MOCVD. Our work underscores a versatile and scalable approach for synthesizing wafer-scale 2D superconductor single crystals, which is essential for their integration into next-generation TMDC-based electronic devices.

Two-dimensional (2D) transition metal dichalcogenides (TMDCs) have been attracting great attention due to their broad range of properties[1], including their use as semiconducting materials (*e.g.*, MoS_2, WS_2) and metallic compounds (*e.g.*, NbS_2, $NbSe_2$). With the rapid advancement of semiconducting TMDC-based electronic devices[2–8], there is an escalating demand for higher performance. However, achieving this is often constrained by the poor interface between 2D materials and conventional 3D contacts[9,10], which hinders efficient charge transfer and overall device efficiency. In this context, metallic TMDCs are considered ideal candidates for 2D metal electrodes due to their van der Waals (vdW) interactions and minimal lattice mismatch with other TMDCs[11–13]. These 2D metal-semiconductor junctions are effective in

A full list of affiliations appears at the end of the paper. e-mail: zhenyu-wang@shu.edu.cn; jzhang@semi.ac.cn; zhangleich@shu.edu.cn; jhzhang@shu.edu.cn

reducing contact resistance by mitigating Fermi level pinning[14], thereby improving electrical performance compared to conventional 3D metal electrodes. Furthermore, metallic TMDCs exhibit intriguing low-temperature phenomena such as superconductivity[15–18], magnetism, and charge density waves (CDWs)[19–23], showing potential applications in quantum computing, spintronics, and nanoscale sensors due to their unique electronic properties and ability to maintain coherence at low temperatures. These interesting electronic properties and prospective applications highlight the importance of developing efficient synthesis methods for 2D metallic and superconducting TMDCs.

In recent years, various approaches have been developed to grow metallic TMDCs, with chemical vapor deposition (CVD) emerging as a particularly promising method. Compared to other techniques[24,25], CVD offers precise control over layer thickness, the ability to grow large areas with high crystallinity[26–30], and the capability to produce heterostructures[31–33]. However, the size of the grown flakes remains constrained, generally within the several to hundred micrometer range, which not only limits the scalability of these materials but also hinders their integration into practical devices that require larger, more uniform films[34–37]. Additionally, due to the lack of a well-established mechanism for controlling the growth of specific crystalline phases, such as the metallic 3R or superconducting 2H phases, achieving the desired electronic properties remains challenging. As a result, the grown samples typically exhibit metallic behavior[38–40] but rarely demonstrate superconductivity. Addressing these challenges is essential for advancing the field and fully harnessing the potential of 2D superconducting TMDCs in next-generation technologies.

Here we demonstrate the epitaxial MOCVD growth of wafer-scale 2D superconducting NbS_2 single-crystal multilayers on a c-plane sapphire. By combining a dual-precursor strategy with a selected sapphire substrate, we achieve wafer-scale multilayer single crystallinity and uniform 2H-phase composition, as verified by atomic force microscopy (AFM), Raman spectroscopy, second-harmonic generation (SHG) mapping, low-energy electron diffraction (LEED), and scanning transmission electron microscopy (STEM). This growth is driven by self-templated concurrent epitaxy, in which lateral expansion and vertical layer addition proceed simultaneously, as supported by our kinetic model. Furthermore, devices fabricated from the NbS_2 film exhibit superconductivity below a transition temperature of 3 K, consistent with a Berezinskii-Kosterlitz-Thouless (BKT) type superconducting phase transition, achieving an impressive yield of 95.1% and a variation of only 12%. Additionally, we demonstrate the MOCVD growth of wafer-scale superconducting $NbSe_2$ films ($T_c = 5$ K), highlighting the versatility and potential of our approach for synthesizing 2D superconductors.

Results

Epitaxial growth of 2D NbS_2 multilayer films by MOCVD

We performed the epitaxial growth of 2D NbS_2 using a home-built metal-organic chemical vapor deposition (MOCVD) system, schematically shown in Supplementary Fig. 1. A 2-inch c-plane sapphire wafer was used as the substrate and pre-annealed in air at 1000 °C for 6 h to generate atomically smooth step terraces (Supplementary Fig. 3), which is essential for epitaxial TMDC growth[27,37,41,42]. Prior to growth, a mixed solution of niobium chloride ($NbCl_5$) and sodium chloride (NaCl) was spin-coated onto the substrate. $NbCl_5$ acted as the initial Nb source, while NaCl facilitated growth by lowering the energy barrier[43] and reducing nucleation density[44]. However, we found that relying solely on $NbCl_5$ is insufficient to achieve continuous wafer-scale single crystals. At the spin-coating concentration employed (0.00125 mol/L), the $NbCl_5$ precursor fails to supply an adequate Nb flux to support full wafer coverage. Conversely, increasing the $NbCl_5$ concentration significantly raises the nucleation density, which disrupts epitaxial alignment and impedes the formation of large-area single-crystal domains. To address this trade-off, we implemented a dual-precursor strategy that decouples nucleation and growth dynamics. The spin-coated $NbCl_5$ locally promotes nucleation with a controlled density, enabling unidirectional alignment of initial domains. Meanwhile, the gaseous $Nb_2(OC_2H_5)_{10}$ provides a continuous and spatially uniform Nb supply during the prolonged growth stage, facilitating the lateral propagation of aligned domains toward full wafer coverage. This combination of a spatially enriched solid precursor and a steady gas-phase feed naturally establishes local chemical-potential gradients that favor subsequent self-templated concurrent epitaxy, as discussed below. Detailed growth conditions are provided in the Methods section and Supplementary Fig. 2.

The growth process consists of four sequential stages, as illustrated in Fig. 1a: initial crystallization at terrace step edges, self-templated epitaxial concurrent growth, inter-domain stitching and grain merging, and finally, the formation of a continuous epitaxial multilayer film across the entire wafer. In the first stage (Fig. 1a(i)), NbS_2 nuclei preferentially form along the terrace step edges of the c-plane sapphire substrate, where the local energy environment favors heterogeneous nucleation, as shown in Fig. 1b. Most nuclei align along the same epitaxial orientation, which can be attributed to the underlying sapphire substrate[27,28,37,41,42]. These nuclei act as a crystalline template, so that subsequent adatom incorporation occurs preferentially on the existing NbS_2 lattice rather than by random secondary nucleation. As growth continues, the small crystals expand laterally along the substrate terraces, forming single-crystal domains from micrometer to millimeter scale (Fig. 1a(ii) and Fig. 1c). At the same time, the well-aligned domains serve as a structural template that directs vertical layer incorporation, allowing the film to thicken while preserving the established in-plane registry, illustrated in Fig. 1f. The multilayer domains exhibit unidirectional alignment, while their lateral expansion is confined by the atomic step edges, leading to the formation of trapezoidal or rectangular shapes (evidenced by AFM image in Fig. 1g). With continued precursor supply, neighboring domains grow and begin to merge (Fig. 1a(iii) and Fig. 1d). In the final stage, domain coalescence proceeds with minimal formation of grain boundaries due to their pre-aligned orientation, eventually yielding a wafer-scale, epitaxially aligned multilayer NbS_2 film. (as shown in Fig. 1a(iv) and Fig. 1e).

To gain quantitative insight into the self-templated concurrent epitaxy, we developed a minimal kinetic model that quantitatively couples the lateral domain expansion and vertical layer accumulation. The total arrival rate of reactive Nb species at the growth front is expressed as $F_{\mathrm{eff}}(t) = F_{\mathrm{seed}} e^{-t/\tau} + F_{\mathrm{gas}}$, where F_{seed} represents the initial Nb flux released from the spin-coated $NbCl_5$ layer, F_{gas} is the continuous gaseous precursor supply during MOCVD, and τ is the decay time of the seed-layer contribution. The lateral growth rate R_L is governed by the adatom diffusion length ℓ and domain size L, approximately following $R_L \propto k_e F_{\mathrm{eff}} \frac{\ell}{L+\ell}$, where k_e is the kinetic coefficient for edge-limited incorporation. The vertical growth rate R_V scales with the terrace capture probability and is given by $R_V \propto k_t F_{\mathrm{eff}} \frac{\ell}{L+\ell}$, where k_t is the kinetic coefficient for surface-limited incorporation. Thus, the competition between R_L and R_V is controlled by two key physical parameters: (i) the flux ratio, $\Gamma = F_{\mathrm{seed}}/(F_{\mathrm{gas}} + F_{\mathrm{seed}})$, which quantifies the relative contribution of seed-layer versus gas-phase supply, and (ii) the normalized diffusion length, $\Lambda = \ell/L_0$, representing the balance between adatom mobility and initial nucleus size. As summarized in the kinetic regime map (Fig. 1h), the film growth transitions from lateral-dominated to vertical-dominated, with an intermediate concurrent epitaxy region. Our experimental dual-precursor conditions fall within this balanced regime, consistent with the observed wafer-scale few-layer single crystallinity. Detailed model parameters and derivations are provided in the Supplementary Information.

https://doi.org/10.1038/s41467-025-67886-z

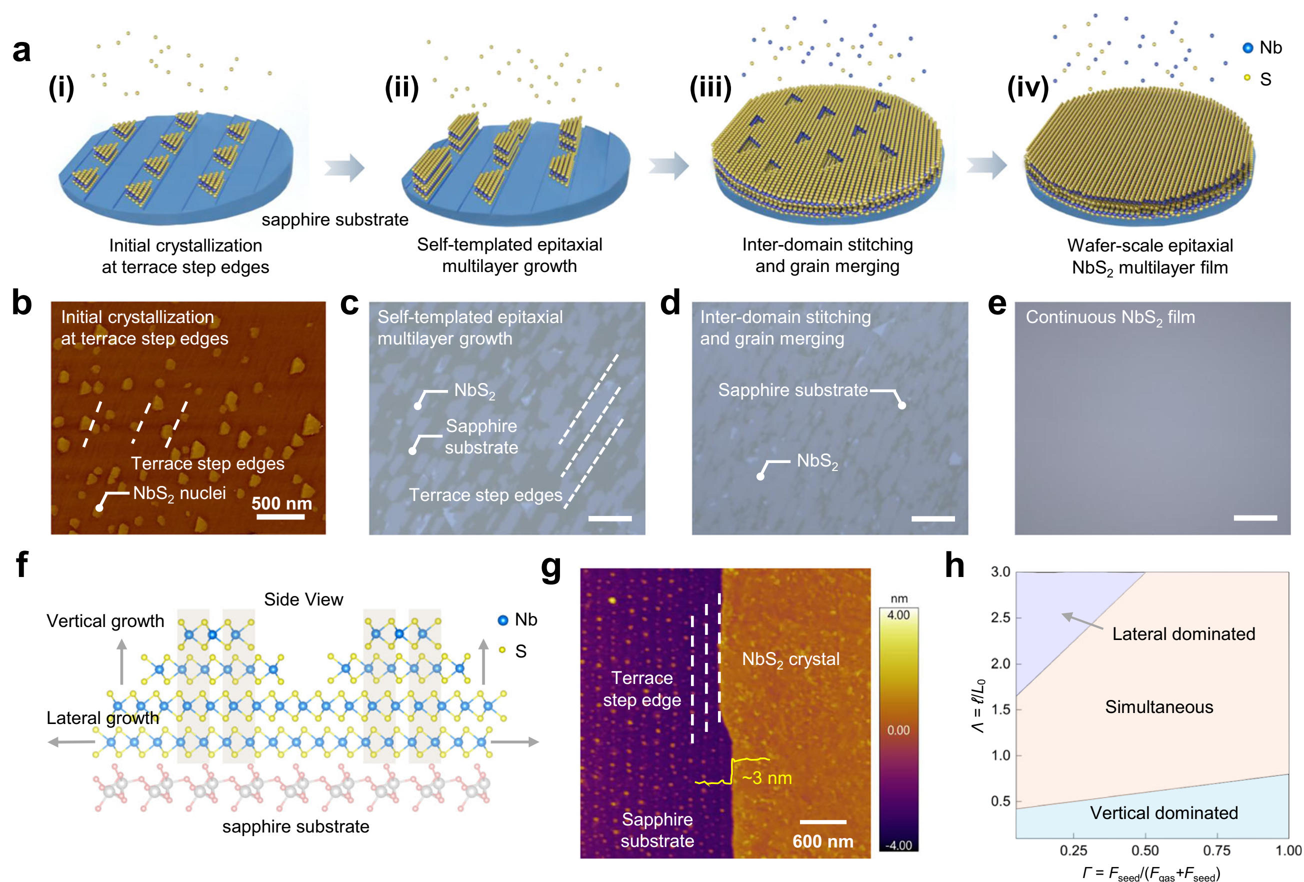

Fig. 1 | Epitaxial growth of wafer-scale NbS_2 films via metal-organic chemical vapor deposition (MOCVD). **a** Schematic illustration of the four-stage epitaxial growth process of NbS_2 on a 2-inch c-plane sapphire wafer: (i) preferential crystallization at terrace step edges; (ii) self-templated epitaxial multilayer growth; (iii) domain merging and grain stitching; and (iv) formation of a continuous epitaxial film. **b**–**e** Atomic force microscopy (AFM) and optical images corresponding to the sequential growth stages illustrated in (**a**). The white dashed lines in (**b**)&(**c**) represent terrace steps on sapphire substrates. Scale bars of (**c**–**e**): 30 µm. **f** Schematic of self-templated concurrent epitaxial growth of NbS_2. Adatoms incorporate both along the basal-plane edges (horizontal arrows) and onto existing terraces (vertical arrows), enabling simultaneous lateral expansion and vertical stacking. **g** High-resolution AFM image showing a single-crystalline NbS_2 domain confined by atomic terrace steps on the sapphire substrate. The white dashed lines represent terrace steps on sapphire substrates, and the height profile of as-grown NbS_2 domain is 3 nm. **h** Calculated phase diagram showing the growth regimes as a function of the precursor flux ratio $\Gamma = F_{seed}/(F_{gas}+F_{seed})$ and the normalized surface diffusion length $\Lambda = \ell/L_0$. F_{seed} represents the initial Nb flux released from the spin-coated $NbCl_5$ layer, F_{gas} is the continuous gaseous precursor supply during MOCVD, ℓ denotes the adatom diffusion length, and L_0 corresponds to the initial nucleus size.

Wafer-scale NbS_2 single crystals

We next investigated the single crystalline and wafer-scale uniformity of the continuous NbS_2 films. Figure 2a displays a typical photograph of wafer-scale NbS_2 single crystals on a 2-inch c-plane sapphire substrate. AFM images obtained from various regions of the 2-inch wafer reveal a smooth surface with a low roughness of less than 100 pm, as illustrated in Fig. 2b(i) and the Supplementary Fig. 6. The absence of grain boundaries in all the AFM images indicates the uniform single-crystalline nature of NbS_2 across the entire wafer, which is further corroborated by additional characterizations discussed below. By intentionally creating a scratch, a clear contrast between the continuous NbS_2 film and the bare sapphire substrate is observed in Fig. 2b(ii). A height profile in Fig. 2b(iii) confirms that the thickness of the as-grown NbS_2 film is approximately 6 nm. Figure 2c illustrates Raman line scans across a 2-inch NbS_2 film on a sapphire wafer, comprising 11 spectra taken at 5 mm steps. The presence of two characteristic peaks, $E^1{}_{2g}$ at 340 cm^{-1} and A_{1g} at 379 cm^{-1}, confirms the 2H phase of NbS_2. While additional modes such as E_1g and E_2g^2 exist in the 2H-NbS_2 phonon dispersion, they are either symmetry-forbidden or Raman-inactive in standard backscattering configurations. Consequently, only the $E^1{}_2$g and A_1g modes are consistently observed with appreciable intensity, which is consistent with prior studies of TMDC single crystals[27,29,37]. Additionally, we performed Raman mapping in several regions of the same wafer (Supplementary Fig. 7). No obvious variations in peak position and intensity were observed in both line scans and 2D mappings, demonstrating the high uniformity of our NbS_2 films. Given that NbS_2 is more prone to oxidation compared to other transition metal dichalcogenides (TMDCs), which could impede further characterization and application, we examined the film post-transfer (Methods). Raman line scans were first performed on the transferred film on a Si/SiO_2 substrate (a typical photograph in Supplementary Fig. 8), with representative spectra shown in Supplementary Fig. 9. The spectra exhibit uniform peak positions and intensities with no detectable shifts, demonstrating that the film remains well preserved after transfer. Complementary XPS analysis was carried out to assess the Nb oxidation state. As shown in Supplementary Fig. 10, the Nb 3*d* spectrum displays the characteristic Nb^{4+} doublet with no discernible Nb^{5+} components, confirming the absence of significant oxidation after transfer.

To further verify the wafer-scale single crystallinity of the NbS_2 films, we performed SHG mapping and LEED measurements. The Fig. 2d(ii), (i) present the SHG mapping and corresponding polarization patterns measured at multiple locations across merging NbS_2 domains. The mapping reveals a strong and spatially uniform SHG

https://doi.org/10.1038/s41467-025-67886-z

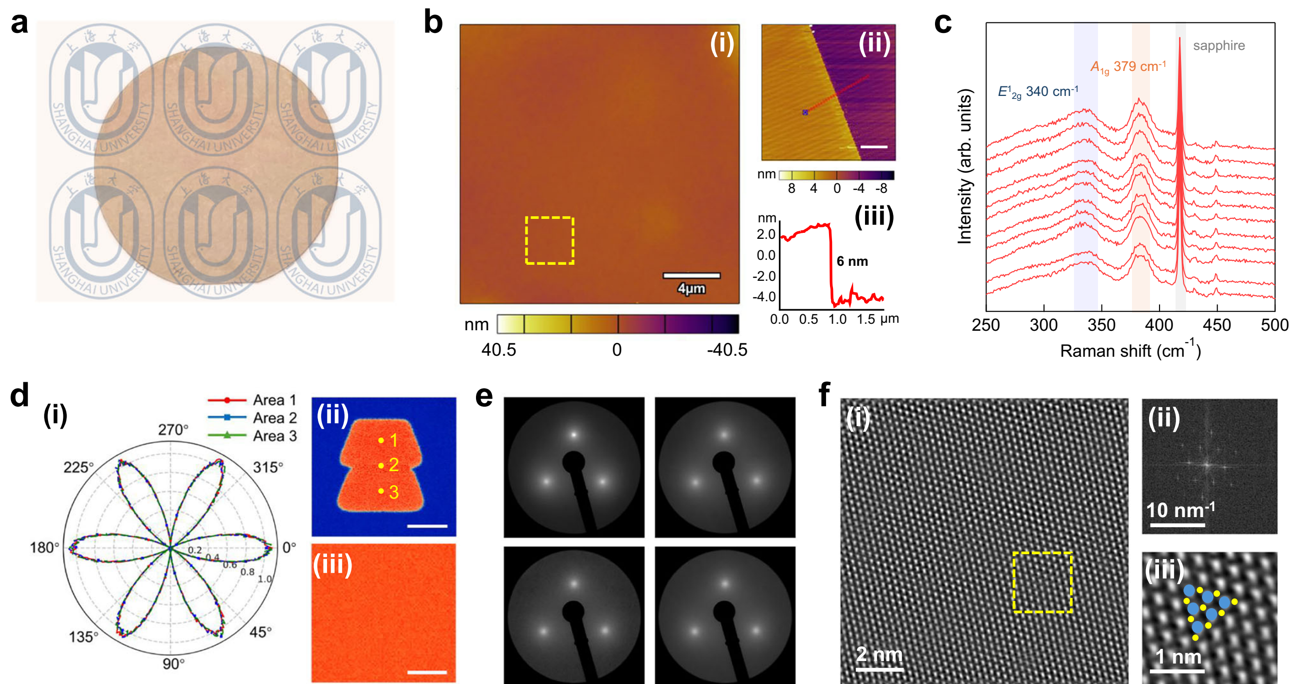

Fig. 2 | Wafer-scale NbS_2 single crystals. **a** A typical photograph showing an as-grown NbS_2 film on a 2-inch sapphire substrate. **b** (i): AFM image of the as-grown NbS_2 film on a sapphire substrate. The root-mean-square (RMS) roughness was extracted from the area outlined by the yellow box by applying first-order flattening and baseline subtraction. (ii): AFM image of the as-grown NbS_2 film on a sapphire substrate, with an intentionally made scratch to show the contrast between NbS_2 and sapphire. Scale bar: 1 µm. (iii): Height profile of the line in (ii), showing the NbS_2 thickness to be around 6 nm. **c** Raman line scans at room temperature for the as-grown 2-inch NbS_2 film on a sapphire substrate, comprising 11 spectra taken at 5 mm steps. **d** (ii) and (iii): Polarization-resolved second-harmonic generation (SHG) mapping on merging NbS_2 domains (Scale bar: 5 µm) and continuous NbS_2 film (Scale bar: 10 µm), respectively. (i): Polar plot (°) of the SHG intensity from three areas shown in (ii). **e** Typical low-energy electron diffraction (LEED) patterns collected from several positions across the 2-inch NbS_2 film. **f** Scanning transmission electron microscopy (STEM) images of the NbS_2 film showing a lattice structure of 2H-polytype stacking and its corresponding fast Fourier transform (FFT) image in (ii). (iii): A zoomed view of the region marked by the yellow dashed box in (i). Blue spheres present Nb atoms, and yellow spheres represent S atoms.

response, and the polarization maxima are identical within experimental uncertainty, confirming the absence of rotational domains or grain boundaries. The Fig. 2d(iii) and Supplementary Fig. 11 further show large-area SHG mapping on continuous NbS_2 film with high intensity uniformity, providing compelling evidence of wafer-scale single crystallinity[28,37,45]. Furthermore, LEED measurements were carried out at multiple positions across the 2-inch wafer[28] (Fig. 2e). All probed regions display identical threefold-symmetric diffraction patterns with the same in-plane orientation, confirming the wafer-scale single crystallinity and epitaxial alignment of the NbS_2 film. The Fig. 2f(i) presents a high-resolution high-angle annular dark-field (HAADF)-STEM image of the NbS_2 film, with the corresponding fast Fourier transform (FFT) image shown in Fig. 2f(ii). A large contamination-free region is visible, displaying a clear lattice arrangement. Upon zooming into the region marked by the yellow square, the lattice structure of 2H NbS_2 features Nb atoms in a trigonal prismatic coordination with S atoms (lattice parameter: a = b = 0.332 nm, c = 1.197 nm), indicative of a 2H-polytype stacking, which corroborates the Raman spectroscopy results. In addition, the same lattice structure was observed in STEM images from various areas of the NbS_2 film, shown in Supplementary Fig. 12. Additionally, we verify the single-crystal nature of our NbS_2 film and the absence of grain boundaries by conducting selected area electron diffraction (SAED) on the several positions across the 2-inch NbS_2 film (top-left panel in Supplementary Fig. 13). In total, 20 areas were examined across the entire TEM grid, and the corresponding SAED patterns are shown in Supplementary Fig. 13. All the SAED patterns show the single crystalline structure with the same lattice orientation, meaning that lattice of all the TEM-probed area is part of one single crystal lattice of NbS_2.

Substrate-guided growth mechanism of 2H-NbS_2

Although NbS_2 can crystallize in both 2H and 3R polytypes, our structural characterizations (see previous section) confirm the exclusive formation of the 2H phase in our MOCVD-grown films. Understanding the underlying mechanisms governing this selective phase formation is essential for the controlled synthesis of desired crystal structures.

To investigate the substrate-guided selective growth of different crystal phases, we compared the epitaxial behaviors of 2H and 3R polytypes of NbS_2 on our growth substrate, c-plane sapphire. As shown in Fig. 3a, both phases consist of stacked 1H layers in which Nb atoms are coordinated in trigonal prismatic sites with surrounding sulfur atoms, and the interlayer spacing is approximately 0.7 nm. The key structural distinction lies in the relative stacking between adjacent layers: 2H-NbS_2 features antiparallel Nb atom alignment across layers, while 3R-NbS_2 exhibits a slight lateral displacement without rotational offset. This subtle difference leads to markedly different interactions with the substrate. C-plane sapphire (α-Al_2O_3) presents a stable hexagonal lattice with close lattice match to the 2H-NbS_2 basal plane, facilitating coherent epitaxial nucleation and lateral propagation. In contrast, the rhombohedral symmetry of the 3R phase introduces lattice mismatch and suppresses ordered growth on this substrate. These differences are further clarified by first-principles calculations (See Supplementary Information).

As illustrated in Fig. 3b, the nucleation process at step edges was modeled by placing initial NbS_2 clusters on a stepped Al_2O_3 surface. The binding energy at nucleation sites (ΔE_1) was found to be significantly lower for 2H-NbS_2 (−0.0216 eV) than for 3R-NbS_2 (−0.0115 eV), indicating that the 2H phase experiences a stronger interfacial interaction and is thermodynamically favored for initial

 https://doi.org/10.1038/s41467-025-67886-z

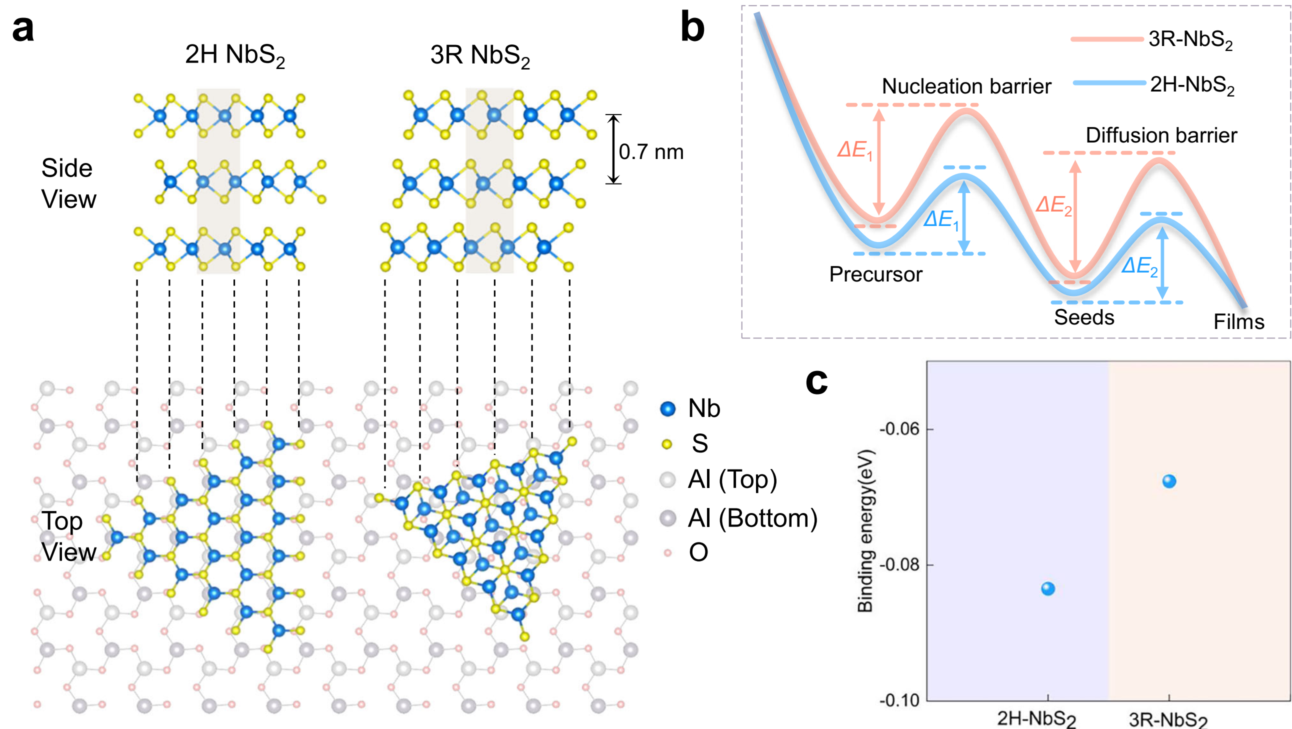

Fig. 3 | Substrate-guided selective growth of 2H-NbS_2. **a** Atomic models of 2H- and 3R-stacked NbS_2 layers on sapphire. Both phases consist of Nb atoms in trigonal prismatic coordination but differ in interlayer stacking. The bottom panel illustrates the epitaxial interface between 2H-NbS_2 and the hexagonal lattice of c-plane sapphire, highlighting lattice symmetrical matching. **b** Schematic diagram of calculated binding energies during growth. ΔE_1 represents the nucleation binding energy at sapphire step edges, and ΔE_2 corresponds to the climbing binding energy during lateral domain propagation. Both energies are more favorable for 2H-NbS_2, indicating enhanced nucleation and adatom incorporation kinetics. **c** Formation energies of 2H- and 3R-NbS_2 on sapphire steps. The 2H phase exhibits a lower formation energy (−0.0835 eV) compared to the 3R phase (−0.0676 eV) at a thickness of 6 nm, confirming its thermodynamic preference on sapphire substrates and explaining the experimental observation of phase-pure 2H-NbS_2 growth.

nucleation. This suggests that the hexagonal symmetry and oxygen-terminated surface of the sapphire promote better lattice registry and orbital overlap with the 2H stacking, stabilizing its early formation. However, the actual nucleation behavior may also be influenced by additional factors, such as local strain accumulation or kinetic limitations during precursor adsorption and diffusion, which could lead to the thickness-dependent phase evolution observed in our previous study[27]. Beyond nucleation, the lateral growth stage was analyzed by evaluating the climbing binding energy (ΔE_2), which reflects the energy cost for edge atoms to incorporate into the advancing crystal front. The 2H phase exhibited a more favorable ΔE_2 (−0.1051 eV) compared to 3R (−0.0792 eV), implying that adatoms diffusing along the step edge can more easily integrate into the 2H lattice. This points to lower kinetic barriers for 2H expansion, which supports continuous lateral growth once nucleation is established.

Additionally, we calculated the total formation energies for the two stacking configurations at a thickness of 6 nm on sapphire steps, as shown in Fig. 3c. The formation energy of 2H-NbS_2 was −0.0835 eV, markedly lower than that of the 3R phase (−0.0676 eV), confirming that the 2H phase (for a thickness of 6 nm) is more stable under growth conditions. This energy difference is attributed to better lattice matching and reduced interfacial strain in the 2H configuration, which aligns with the experimental observation of single-phase 2H-NbS_2. Although phase formation may also be influenced by kinetic factors and other growth conditions, the calculated energy difference (~16 meV per formula unit) is consistent in magnitude with values reported in prior studies[46,47] for stacking-dependent stability in layered TMDCs and represents an important contributing factor to the observed 2H phase selectivity.

Electrical transport in 2D wafer-scale NbS_2

To characterize the electrical transport properties of the MOCVD-grown 2-inch NbS_2 film (thickness = 6 nm), an array of multiterminal devices was fabricated after transferring the samples onto a Si/SiO_2 substrate, as shown in Fig. 4a. The inset of Fig. 4a provides a zoomed view of a multiterminal device, where a stack of Ti/Au was deposited on top of NbS_2 to serve as drain and source electrodes, as well as probes. The detailed fabrication process is described in the Methods section.

By performing a typical four-terminal *V*–*I* measurement illustrated in the inset of Fig. 4b, the resistance of NbS_2 between probe 1 and 2 (R_{12}) can be calculated as a value of around 20 Ω at room temperature, indicating its metallic behavior. Figure 4c shows the resistance distribution of 144 NbS_2 devices within a 1.2×0.9 cm^2 area depicted in Fig. 4a. Due to the high uniformity of our NbS_2 film, we achieved a device yield of 95.1% (137 functional devices out of 144) and a resistance variation of 12%, defined as the ratio of the standard deviation ($\sigma = 2.7\ \Omega$) to the mean of the resistance values ($\mu = 22.6\ \Omega$), across a centimeter range. These results are comparable with values reported for CVD-grown 2D materials[29,37], suggesting that the observed spread mainly originates from polymer contamination or local fabrication-related defects rather than intrinsic film nonuniformity.

Since our NbS_2 exhibits the 2H phase, as confirmed by Raman and STEM measurements in Fig. 2, and 2H phase NbS_2 is known to behave as a superconductor at low temperatures, we further investigated its superconducting properties by measuring its resistance (R_{12}) as a function of temperature in zero magnetic field. As shown in Fig. 4d, the resistance decreases linearly with decreasing temperature down to 3.5 K due to its metallic nature. Upon further cooling from around 3.5 K, the resistance sharply drops to zero, indicating the superconducting transition. A residual resistance ratio (*RRR*) of around 8,

 https://doi.org/10.1038/s41467-025-67886-z

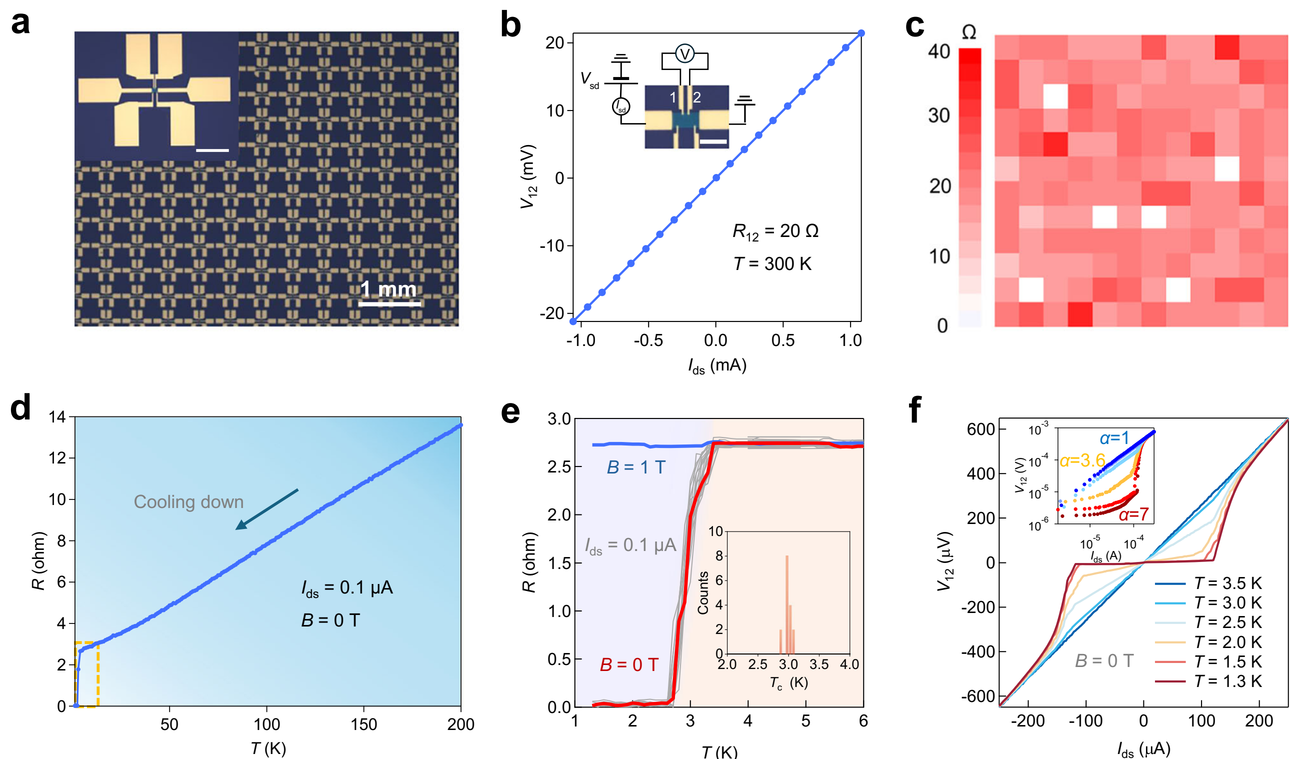

Fig. 4 | Electrical performance of wafer-scale NbS_2 film. a Optical microscope image of an array of multiterminal devices fabricated after transferring the NbS_2 film onto a Si/SiO_2 substrate. Inset: A zoomed view of a multiterminal device. Scale bar: 100 µm. **b** Four-terminal V–I curve of a NbS_2 device at room temperature, showing a resistance value of 20 Ω. Inset: Illustration of the four-terminal measurements. V_{12} represents the voltage measured at the probes of 1&2. V_{sd} represents the source-drain voltage, and I_{sd} represents the source-drain current. Scale bar: 20 nm. **c** The resistance (R_{12}) distribution of 144 NbS_2 devices within a 1.2 × 0.9 cm² area presented in (**a**). The measurement was conducted at 300 K. **d** Resistance (R_{12}) as a function of temperature in zero magnetic field, cooling down from 200 K to 1.3 K. The yellow dashed box marks a temperature range around superconducting transition temperature (T_c). **e** The resistance of 16 NbS_2 devices as they are cooled from 6 K to 1.3 K in the absence of a magnetic field (red and gray curves) and in a magnetic field of 1 T (blue curve). Inset: Spatial distribution of T_c across 16 NbS_2 devices, exhibiting a narrow variation range of ±0.1 K. **f** Four-terminal V–I curve of a NbS_2 device at various temperatures from 3.5 K to 1.3 K in the absence of a magnetic field. Inset: V–I curve in (**f**) replotted on a logarithmic scale showing $V \propto I^{\alpha}$ behavior, consistent with the expected Berezinskii-Kosterlitz-Thouless (BKT) model. The extracted power-law exponents (α) are indicated in the corresponding colors.

defined as the ratio between the resistance at $T = 300$ K and the normal-state resistance above the superconducting transition temperature, can be calculated. This high *RRR* value indicates the high crystalline quality of our NbS_2 superconductor in terms of its electrical behavior.

Figure 4e presents the resistance of 16 NbS_2 devices as they are cooled from 6 K in the absence of a magnetic field (red and gray curves), together with the distribution of their critical temperatures (T_c), defined as the temperature where the resistance reaches half of the normal-state resistance (R_N), *i.e.*, $R(T_c) = 0.5\ R_N$. All devices display nearly identical superconducting transitions, with $T_c = 3.0 \pm 0.1$ K, highlighting the high uniformity of superconductivity across the NbS_2 film. When a magnetic field of 1 T is applied (blue curve), the NbS_2 devices exhibit metallic behavior without a resistance drop, indicating that the superconductivity is entirely suppressed by the magnetic field. Furthermore, we evaluated the environmental stability of the NbS_2 devices by monitoring their temperature-dependent resistance over time (see Supplementary Fig. 15). The superconducting properties remain unchanged after 30 days in a high-purity helium environment, indicating high long-term stability under cryogenic and oxygen-free conditions. In contrast, when exposed to ambient air, the superconducting transition gradually degrades and disappears entirely after 10 days, highlighting the strong sensitivity of NbS_2 to oxidation.

Figure 4f depicts the four-probe I–V characterization of the NbS_2 device across various temperatures without a magnetic field applied. At 3.5 K, the device shows linear Ohmic behavior with a resistance of around 2.7 Ω, consistent with the metallic normal-state resistance. As the temperature decreases further, the I–V curve becomes non-linear near the critical current gap, revealing varying resistance values. A critical current gap of around ±145 µA can be estimated by plotting dV/dI as a function of I_{ds} for the curves at various temperatures, as shown in Supplementary Fig. 16. The curve exhibits a sharp peak at the critical current, signifying the transition from the normal resistive state to the superconducting zero-resistance state. Furthermore, the logarithmic scale inset of the V–I curves illustrates a transition from a linear V–I relationship to a power-law dependence ($V \propto I^{\alpha}$), consistent with a BKT type superconducting phase transition. The BKT transition temperature (T_{BKT}) can be estimated to be 3.0 K, corresponding to an α value of 3 for our NbS_2 crystal, which aligns well with the R–T results presented in Fig. 4e. These findings emphasize that our MOCVD-grown 2-inch NbS_2 film exhibits the characteristics expected of a 2D superconductor.

Other than NbS_2, we further demonstrate the generalizability of our growth strategy by achieving the epitaxial synthesis of 2H-$NbSe_2$ single crystals on sapphire substrates (Supplementary Fig. 17). Structural and morphological characterizations, including optical microscopy, AFM, TEM and Raman spectroscopy, confirm the high crystallinity, phase purity, and large-area uniformity of the as-grown $NbSe_2$ films. Low-temperature transport measurements (Supplementary Fig. 17f) reveal a sharp superconducting transition at $T_c \approx 5$ K, which is entirely suppressed under an external magnetic field of 1.5 T, confirming the intrinsic superconducting nature of the 2H-$NbSe_2$.

Discussion

In conclusion, we have demonstrated the epitaxial MOCVD growth of wafer-scale 2D superconducting NbS_2 and $NbSe_2$ single-crystal multilayers on c-plane sapphires. A combination of dual-precursor strategy and sapphire substrate selection enables self-templated concurrent epitaxy to yield uniform 2H-phase films, which is quantitatively supported by our kinetic model. Moreover, devices fabricated from these NbS_2 films exhibited superconductivity below a transition temperature of 3 K ($T_{c\ (NbSe2)} = 5$ K), consistent with a BKT type superconducting phase transition, yielding an impressive 95.1% success rate with only 12% resistance variation. Our findings demonstrate a practical and scalable method for producing wafer-scale 2D superconductor single crystals, which provides the platform for their widespread use in next-generation TMDC-based electronic devices.

Methods

Material synthesis

Our NbS_2 single crystal films were synthesized using a home-built MOCVD system, as illustrated in Supplementary Fig. 1. A 2-inch c-plane sapphire wafer was used as growth substrate and annealed in air at 1000 °C for 6 h. A mixed solution was prepared by dissolving niobium chloride ($NbCl_5$, 0.00125 mol/L) and sodium chloride (NaCl, 0.1 mol/L) in isopropanol (IPA). The mixture was ultrasonicated for 15 min to ensure high dispersion quality and then spin-coated onto the sapphire substrate before loading it into the growth chamber. The reactor tube was purged with argon to remove any residual oxygen and humidity before growth. The furnace was first heated to 850 °C and maintained for 10 min while H_2S was introduced into the chamber with argon as the carrier gas, allowing the pre-coated $NbCl_5$ to react with H_2S and form initial NbS_2 seeds. The temperature then increased to 950 °C and held for 20 min, during which the NbS_2 domains expanded with continuous H_2S supply. Finally, the furnace was heated to 980 °C, and niobium ethoxide ($Nb_2(OC_2H_5)_{10}$) was introduced as a gaseous precursor, carried by 10 sccm of argon, further promoting the lateral growth of NbS_2. A 4 sccm flow of hydrogen (H_2) was used to reduce carbon contamination. Throughout the process, argon and H_2S were supplied at a flow rate of 200 sccm and 30 sccm, respectively, with the growth conducted at 800 mbar. After the growth was completed, the chamber was allowed to cool naturally, with the H_2S flow reduced to 5 sccm until the furnace temperature reached 150 °C to minimize sulfur vacancies.

Our $NbSe_2$ single crystal films were synthesized using the same MOCVD system and substrate preparation procedures as those employed for NbS_2. The main differences in growth conditions lie in the growth temperature and the choice of gaseous precursors, as described below. The furnace was first heated to 900 °C and maintained for 10 min while H_2Se[48] was introduced into the chamber, allowing the pre-coated $NbCl_5$ to react with H_2Se and form initial $NbSe_2$ seeds. The temperature was then increased to 950 °C and held for 20 min, during which the $NbSe_2$ domains expanded under continuous H_2Se supply. Finally, the furnace was heated to 990 °C, and niobium ethoxide ($Nb_2(OC_2H_5)_{10}$) was introduced as a gaseous precursor, carried by 8 sccm of argon, to further promote lateral domain growth. A 6 sccm flow of hydrogen (H_2) was used to reduce carbon contamination. Throughout the process, argon and H_2Se were supplied at flow rates of 200 sccm and 25 sccm, respectively. The growth was conducted at a pressure of 800 mbar. After the growth was completed, the chamber was allowed to cool naturally.

Optical characterization

Raman spectra and mapping were obtained using a Renishaw inVia Confocal Raman Microscope. The spectra were collected with a 532 nm laser and a 3000 g/mm grating at room temperature. The excitation spot size was approximately 1 μm with a laser power of 1 mW.

LEED measurements were performed using an OCI MCP-LEED system at room temperature in an ultrahigh vacuum of 10^{-10} torr. The electron acceleration voltage was 240 eV for LEED.

SHG mapping was performed in a Spectra-Physics InSight system under excitation from a femtosecond laser centred at 820 nm with an average power of 800 μW.

AFM measurements were performed using an Asylum Research system to evaluate the surface morphology and roughness of the films. The root-mean-square (RMS) roughness was computed on representative areas of the wafer from a 5 μm × 5 μm flattened window using the Asylum Research analysis software.

Scanning transmission electron microscopy measurements

The as-grown samples were first transferred onto a silicon nitride TEM grid by using the following approach: The samples were first spin-coated with PMMA (poly(methyl methacrylate)) A4 at 2000 rpm for 60 s and then heated on a hot plate at 180 °C for 5 min to dry. After immersing in water for 5 min, the PMMA film with the samples was detached by water tension and transferred using a silicon nitride TEM grid. The samples were then baked on a hot plate at 65 °C for 10 min to dry and enhance adhesion. Finally, the PMMA film was removed by immersing in acetone overnight, followed by annealing in high vacuum at 250 °C for 6 h.

High-resolution high-angle annular dark field (HAADF) STEM imaging was conducted using a double aberration-corrected FEI Titan Themis microscope. The beam convergence half-angle was set to 20 mrad, corresponding to a HAADF detector collection angle of 49.5–198 mrad. The microscope operated at an accelerating voltage of 80 kV, below the threshold for electron-beam induced knock-on damage of the samples. The electron probe current was set to around 20 pA. To prevent sample drift, images were acquired at various locations using a faster scan with 512 × 512 pixels and 8 μs dwell times.

Wafer-scale sample transfer

To transfer the wafer-scale NbS_2 film from the sapphire substrate, the sample was spin-coated with PMMA (poly(methyl methacrylate)) A4 at 2000 rpm for 1 min and then baked on a hot plate at 180 °C for 10 min for drying. The edges of the PMMA layer were carefully scratched with a sharp tweezer, and the sample was then covered with thermal-release tape to provide additional mechanical support and immersed in water for 15 min. The PMMA layer, along with the NbS_2 film, detached from the sapphire substrate and adhered to the thermal-release tape. To minimize film wrinkling and mechanical damage during transfer, the sample was gently dried with a nitrogen gun and visually inspected to avoid large bubbles or delamination. It was then attached to the target Si/SiO_2 substrate, using a tweezer to remove any bubbles between the sample and the substrate. To promote adhesion, the sample was baked again on a hot plate at 55 °C for 1 h. The thermal-release tape was then removed by increasing the baking temperature to 135 °C. Finally, the sample was immersed in acetone overnight and annealed in high vacuum at 250 °C for 6 h to remove PMMA residue and eliminate trapped interfacial bubbles.

Device fabrication

The samples were first transferred onto a 4-inch Si/SiO_2 substrate before undergoing fabrication. The samples were then etched into the desired geometry using laser writer photolithography (utilizing LOR 5 A and AZ 1512 HS as photoresist layers) and a XeF_2 chemical etcher. The photoresist layers were cleaned by immersing them in dimethyl sulfoxide (DMSO) overnight. Laser writer photolithography was used again to pattern the electrodes. Finally, a stack of 2 nm/80 nm thick Ti/Au was deposited by e-beam evaporation to form the electrodes, followed by a lift-off process in DMSO to remove the photoresist layer. Between fabrication steps, the samples were kept in an inert Ar

environment inside a glovebox to prevent degradation from exposure to air.

Transport measurements

Cryogenic electrical transport measurements were conducted using an ICE Oxford liquid helium continuous flow system, achieving a base temperature of approximately 1.4 K. *V–I* characteristics were obtained by applying a constant DC current via a Keithley 2636b sourcemeter, while simultaneously measuring the DC voltage with a Keithley 2182a nanovoltmeter.

First-principles modeling

Density functional theory (DFT) calculations were conducted using the VASP package to investigate the thermodynamic preference between 2H and 3R phases of NbS_2 on c-plane sapphire. Stepped sapphire surfaces were modeled to simulate nucleation and lateral growth processes. Binding energies, climbing energies, and formation energies were computed by comparing the total energies of combined and isolated systems.

To complement the first-principles calculations, we developed a minimal kinetic model to capture the coupled lateral and vertical growth dynamics. Numerical integration of the rate equations was performed using Python with the NumPy and SciPy libraries, while parameter sweeps and regime-map generation were carried out with custom scripts. All simulations and figure generation were implemented in Python/Matplotlib, and full details of the equations and parameters are provided in Supplementary Information.

Data availability

The Source Data underlying the figures of this study are available with the paper. All raw data generated during the current study are available from the corresponding authors upon request. Source data are provided with this paper.

References

1. Manzeli, S., Ovchinnikov, D., Pasquier, D., Yazyev, O. V. & Kis, A. 2D transition metal dichalcogenides. *Nat. Rev. Mater.* **2**, 1–15 (2017).
2. Jayachandran, D. et al. Three-dimensional integration of two-dimensional field-effect transistors. *Nature* **625**, 276–281 (2024).
3. Fiori, G. et al. Electronics based on two-dimensional materials. *Nat. Nanotech.* **9**, 768–779 (2014).
4. Yin, L., Cheng, R., Wen, Y., Liu, C. & He, J. Emerging 2D memory devices for in-memory computing. *Adv. Mater.* **33**, 2007081 (2021).
5. Migliato Marega, G. et al. Logic-in-memory based on an atomically thin semiconductor. *Nature* **587**, 72–77 (2020).
6. Tang, J. et al. Low power flexible monolayer MoS_2 integrated circuits. *Nat. Commun.* **14**, 3633 (2023).
7. Das, S. et al. Transistors based on two-dimensional materials for future integrated circuits. *Nat. Electron* **4**, 786–799 (2021).
8. Chen, S. et al. Channel and contact length scaling of two-dimensional transistors using composite metal electrodes. *Nat. Electron* **8**, 394–402 (2025).
9. Allain, A., Kang, J., Banerjee, K. & Kis, A. Electrical contacts to two-dimensional semiconductors. *Nat. Mater.* **14**, 1195–1205 (2015).
10. Kim, C. et al. Fermi level pinning at electrical metal contacts of monolayer molybdenum dichalcogenides. *ACS Nano* **11**, 1588–1596 (2017).
11. Geim, A. K. & Grigorieva, I. V. Van der Waals heterostructures. *Nature* **499**, 419–425 (2013).
12. Novoselov, K. S., Mishchenko, A., Carvalho, A. & Castro Neto, A. H. 2D materials and van der Waals heterostructures. *Science* **353**, aac9439 (2016).
13. Ding, X. et al. NbS2: a promising p-type ohmic contact for two-dimensional materials. *Phys. Rev. Appl.* **12**, 064061 (2019).
14. Liu, Y., Stradins, P. & Wei, S.-H. Van der Waals metal-semiconductor junction: weak fermi level pinning enables effective tuning of Schottky barrier. *Sci. Adv.* **2**, e1600069 (2016).
15. Guillamón, I. et al. Superconducting density of states and vortex cores of 2H-NbS2. *Phys. Rev. Lett.* **101**, 166407 (2008).
16. Nagata, S. et al. Superconductivity in the layered compound 2H-TaS_2. *J. Phys. Chem. Solids* **53**, 1259–1263 (1992).
17. Revolinsky, E., Spiering, G. A. & Beerntsen, D. J. Superconductivity in the niobium-selenium system. *J. Phys. Chem. Solids* **26**, 1029–1034 (1965).
18. Freitas, D. C. et al. Strong enhancement of superconductivity at high pressures within the charge-density-wave states of 2H-TaS2 and 2H-TaSe2. *Phys. Rev. B* **93**, 184512 (2016).
19. Calandra, M., Mazin, I. I. & Mauri, F. Effect of dimensionality on the charge-density wave in few-layer 2H-NbSe2. *Phys. Rev. B* **80**, 241108 (2009).
20. Chatterjee, U. et al. Emergence of coherence in the charge-density wave state of 2H-$NbSe_2$. *Nat. Commun.* **6**, 6313 (2015).
21. Xi, X. et al. Strongly enhanced charge-density-wave order in monolayer NbSe2. *Nat. Nanotech.* **10**, 765–769 (2015).
22. Leroux, M., Cario, L., Bosak, A. & Rodière, P. Traces of charge density waves in NbS_2. *Phys. Rev. B* **97**, 195140 (2018).
23. Rossnagel, K. et al. Fermi surface of 2H-$NbSe_2$ and its implications on the charge-density-wave mechanism. *Phys. Rev. B* **64**, 235119 (2001).
24. Hotta, T. et al. Molecular beam epitaxy growth of monolayer niobium diselenide flakes. *Appl. Phys. Lett.* **109**, 133101 (2016).
25. Li, Z. et al. Thermodynamics and kinetics synergy for controlled synthesis of 2D van der Waals single-crystal $NbSe_2$ via modified chemical vapor transport. *Cryst. Growth Des.* **20**, 706–712 (2020).
26. Wang, H. et al. High-quality monolayer superconductor $NbSe_2$ grown by chemical vapour deposition. *Nat. Commun.* **8**, 394 (2017).
27. Wang, Z. et al. Superconducting 2D NbS_2 grown epitaxially by chemical vapor deposition. *ACS Nano* **15**, 18403–18410 (2021).
28. Wang, J. et al. Dual-coupling-guided epitaxial growth of wafer-scale single-crystal WS_2 monolayer on vicinal a-plane sapphire. *Nat. Nanotechnol.* **17**, 33–38 (2022).
29. Jiang, H. et al. Two-dimensional Czochralski growth of single-crystal MoS_2. *Nat. Mater.* **24**, 188–196 (2025).
30. Liu, L. et al. Homoepitaxial growth of large-area rhombohedral-stacked MoS_2. *Nat. Mater.* **24**, 1195–1202 (2025).
31. Fu, Q. et al. One-step synthesis of metal/semiconductor heterostructure NbS_2/MoS_2. *Chem. Mater.* **30**, 4001–4007 (2018).
32. Zhang, Y. et al. Edge-epitaxial growth of 2D NbS_2-WS_2 lateral metal-semiconductor heterostructures. *Adv. Mater.* **30**, 1803665 (2018).
33. Wang, Z. et al. Substitutional p-type doping in NbS_2–MoS_2 lateral heterostructures grown by MOCVD. *Adv. Mater.* **35**, 2209371 (2023).
34. Xu, X. et al. Growth of 2D materials at the wafer scale. *Adv. Mater.* **34**, 2108258 (2022).
35. Li, X. et al. Controlled synthesis and accurate doping of wafer-scale 2D semiconducting transition metal dichalcogenides. *Adv. Mater.* **37**, 2305115 (2025).
36. Chen, J. et al. Synthesis of wafer-scale monolayer WS_2 crystals toward the application in integrated electronic devices. *ACS Appl. Mater. Interfaces* **11**, 19381–19387 (2019).
37. Li, T. et al. Epitaxial growth of wafer-scale molybdenum disulfide semiconductor single crystals on sapphire. *Nat. Nanotechnol.* **16**, 1201–1207 (2021).
38. Wang, X. et al. Chemical vapor deposition of trigonal prismatic NbS_2 monolayers and 3R-polytype few-layers. *Nanoscale* **9**, 16607–16611 (2017).
39. Kozhakhmetov, A., Choudhury, T. H., Al Balushi, Z. Y., Chubarov, M. & Redwing, J. M. Effect of substrate on the growth and properties of

thin 3R NbS_2 films grown by chemical vapor deposition. *J. Cryst. Growth* **486**, 137–141 (2018).
40. Zhao, S. et al. Two-dimensional metallic NbS_2: growth, optical identification and transport properties. *2D Mater.* **3**, 025027 (2016).
41. Dumcenco, D. et al. Large-area epitaxial monolayer MoS_2. *ACS Nano* **9**, 4611–4620 (2015).
42. Liu, L. et al. Uniform nucleation and epitaxy of bilayer molybdenum disulfide on sapphire. *Nature* **605**, 69–75 (2022).
43. Yang, P. et al. Batch production of 6-inch uniform monolayer molybdenum disulfide catalyzed by sodium in glass. *Nat. Commun.* **9**, 979 (2018).
44. Kim, H., Ovchinnikov, D., Deiana, D., Unuchek, D. & Kis, A. Suppressing nucleation in metal–organic chemical vapor deposition of MoS_2 monolayers by alkali metal halides. *Nano Lett.* **17**, 5056–5063 (2017).
45. Huang, W., Xiao, Y., Xia, F., Chen, X. & Zhai, T. Second harmonic generation control in 2D layered materials: status and outlook. *Adv. Funct. Mater.* **34**, 2310726 (2024).
46. Van Winkle, M. et al. Rotational and dilational reconstruction in transition metal dichalcogenide moiré bilayers. *Nat. Commun.* **14**, 2989 (2023).
47. He, J. Stacking effects on the electronic and optical properties of bilayer transition metal dichalcogenides. *Phys. Rev. B* **89**, 075409 (2014).
48. Zhu, H. et al. Step engineering for nucleation and domain orientation control in WSe_2 epitaxy on c-plane sapphire. *Nat. Nanotechnol.* **18**, 1295–1302 (2023).
49. Momma, K. & Izumi, F. *VESTA 3* for three-dimensional visualization of crystal, volumetric and morphology data. *J. Appl. Crystallogr.* **44**, 1272–1276 (2011).

Acknowledgements

This work was financially supported by the Research Funding provided by Shanghai University, the National Key Research and Development Program of China (Grant Nos. 2022YFA1405100, 2024YFA1409700), the Beijing Natural Science Foundation Key Program (Grant No. Z220005), the Natural Science Foundation of Shanghai (Grant No. 25ZR1402166), the Fundamental Research Program of Shanghai (Grant No. 25JD1401600) and the National Natural Science Foundation of China (Grant Nos. 92577126, 12241405, 52502190). The atomic structures shown on Figs. 1f and 3a were drawn using VESTA[49].

Author contributions

Jianhua, Z., Lei, Z. and Z.W. initiated and supervised the work. T.L. performed the MOCVD growth under supervision of Jianhua, Z., Lei, Z. and Z.W. T.L., X.C., and Z.Z., fabricated the devices with supervision of Z.W. and Le Z. Z.W. designed and performed electrical measurements with support of A.K. T.L., Y.H. and J.L. performed material characterizations under supervision of Jianhua Z., M.L. and Z.W. L.S. and Z.Y. performed simulation with supervision of Lei, Z., Jing, Z., and Z.W. Z.W., T.L., and L.S. analyzed the data with input from Jianhua, Z., Lei, Z., and A.K. All the authors contributed to the writing of the manuscript.

Competing interests

The authors declare no competing interests.

Additional information

Supplementary information The online version contains supplementary material available at https://doi.org/10.1038/s41467-025-67886-z.

Correspondence and requests for materials should be addressed to Zhenyu Wang, Jing Zhang, Lei Zhang or Jianhua Zhang.

Peer review information *Nature Communications* thanks the anonymous reviewers for their contribution to the peer review of this work. A peer review file is available.

Reprints and permissions information is available at http://www.nature.com/reprints

Publisher's note Springer Nature remains neutral with regard to jurisdictional claims in published maps and institutional affiliations.

Open Access This article is licensed under a Creative Commons Attribution-NonCommercial-NoDerivatives 4.0 International License, which permits any non-commercial use, sharing, distribution and reproduction in any medium or format, as long as you give appropriate credit to the original author(s) and the source, provide a link to the Creative Commons licence, and indicate if you modified the licensed material. You do not have permission under this licence to share adapted material derived from this article or parts of it. The images or other third party material in this article are included in the article's Creative Commons licence, unless indicated otherwise in a credit line to the material. If material is not included in the article's Creative Commons licence and your intended use is not permitted by statutory regulation or exceeds the permitted use, you will need to obtain permission directly from the copyright holder. To view a copy of this licence, visit http://creativecommons.org/licenses/by-nc-nd/4.0/.

© The Author(s) 2025

[1]School of Microelectronics, Shanghai University, Shanghai, China. [2]Sino-Swiss Institute of Advanced Technology (SSIAT), Shanghai University, Shanghai, China. [3]Electrical Engineering Institute, École Polytechnique Fédérale de Lausanne (EPFL), Lausanne, Switzerland. [4]Institute of Materials Science and Engineering, École Polytechnique Fédérale de Lausanne (EPFL), Lausanne, Switzerland. [5]State Key Laboratory of Semiconductor Physics and Chip Technologies, Institute of Semiconductors, Chinese Academy of Sciences, Beijing, China. [6]College of Materials Science and Opto-Electronic Technology, University of Chinese Academy of Sciences, Beijing, China. [7]These authors contributed equally: Zhenyu Wang, Tan Luo, Liu Shi, Xin Chen.
e-mail: zhenyu-wang@shu.edu.cn; jzhang@semi.ac.cn; zhangleich@shu.edu.cn; jhzhang@shu.edu.cn